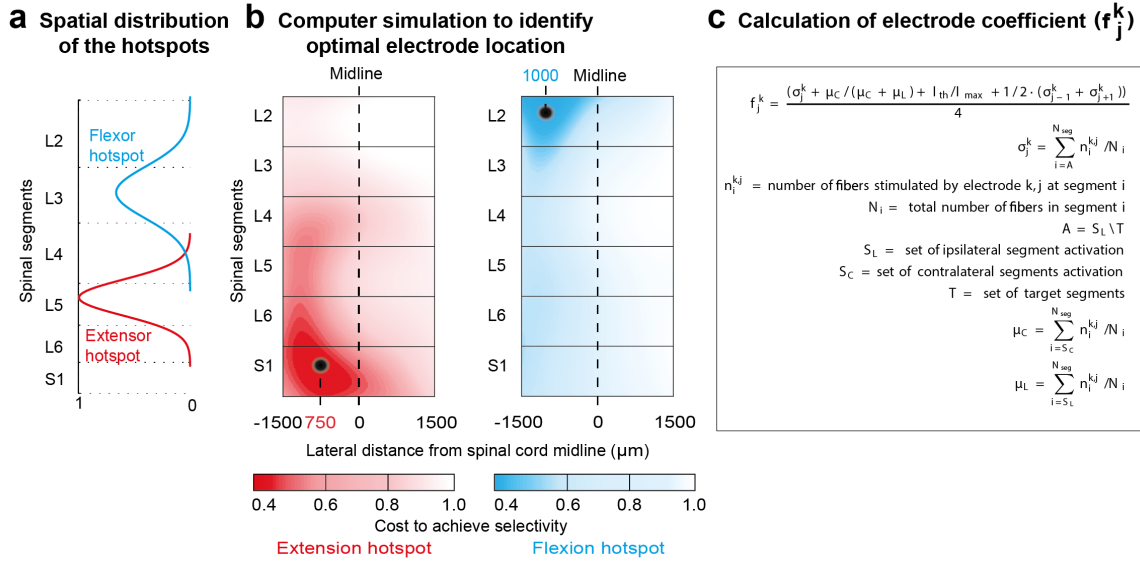Supplementary Figure 1: Spatial distribution of hindlimb motoneurons and 3D reconstruction of vertebrae, spinal cord and dorsal roots in Lewis rats

(**a**) Plots reporting the relative spatial distribution of motoneuron density along the rostrocaudal extent of lumbosacral segments for each traced muscle. Each distribution is the average (+/- SEM) of motoneuron densities calculated for 2 to 3 rats per muscle. The density is normalized to the total number of detected motoneurons for each muscle and rat, which corresponds to 1. (**b**) Quantification of the length of vertebra T12 to L3–L4, and of spinal segments L1 to S1 in three rats. The vertical bars on each diagram indicate the standard deviation of measurements across rats. The photographs show coronal views of the entire half of the spinal cord, including the dura mater, dorsal roots, and spinal tissue. The complementary views show camera Lucida reconstructions of the white and grey matter, and of the dorsal roots. Coronal sections were extracted from spinal segments L3 and S1. The dorsal roots projecting to L2 and S1 spinal segments are color-coded to visualize their respective location. (**c**) 3D reconstruction of the entire lumbosacral spinal cord and dorsal roots. The dorsal roots innervating L2 and S1 spinal segments are color-coded to help visualizing their respective spatial trajectory. The 3D reconstructions are displayed from a dorsal view, and from a view that is rotated by 45 ° leftward around the rostrocaudal axis in order to visualize the trajectory of the dorsal roots along spinal segments. The color-coded dots indicate the locations of electrodes targeting extensor and flexor hotspots through the recruitment of dorsal roots.
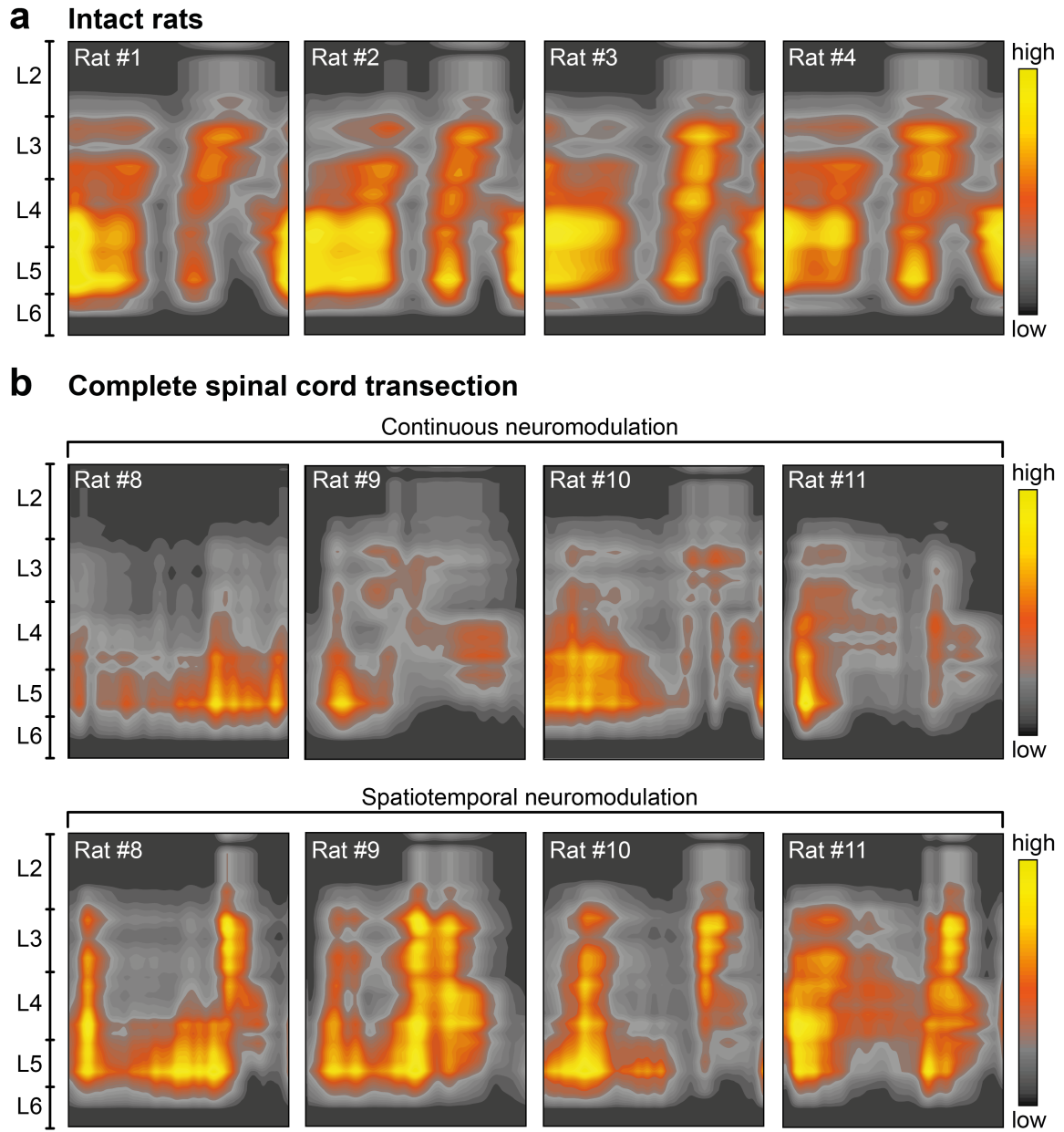
Supplementary Figure 2: Spatiotemporal maps of motoneuron activation
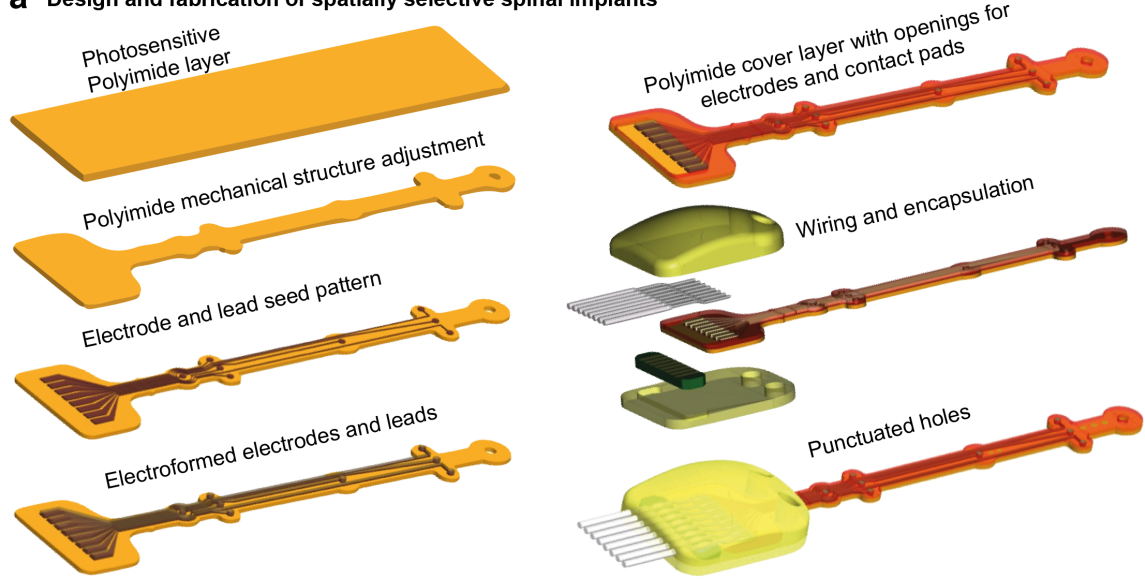(**a**) Spatiotemporal map of motoneuron activation recorded in four intact rats. (**b**) Spatiotemporal map of motoneuron activation recorded in four rats with complete SCI during continuous versus spatiotemporal neuromodulation.
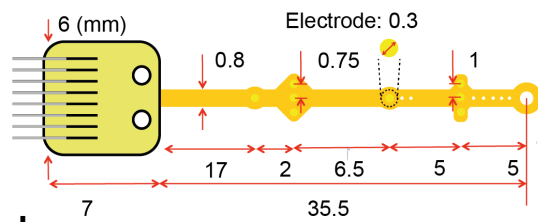
a Spatial distribution of the hotspots

b Computer simulation to identify optimal electrode location

c Calculation of electrode coefficient (f_j^k)

$$f_j^k = \frac{(\sigma_j^k + \mu_C/(\mu_C + \mu_L) + I_{th}/I_{max} + 1/2 \cdot (\sigma_{j-1}^k + \sigma_{j+1}^k))}{4}$$

$$\sigma_j^k = \sum_{i=A}^{N_{seg}} n_i^{k,j}/N_i$$

$n_i^{k,j}$ = number of fibers stimulated by electrode k,j at segment i

N_i = total number of fibers in segment i

$A = S_L \setminus T$

S_L = set of ipsilateral segment activation

S_C = set of contralateral segments activation

T = set of target segments

$$\mu_C = \sum_{i=S_C}^{N_{seg}} n_i^{k,j}/N_i$$

$$\mu_L = \sum_{i=S_L}^{N_{seg}} n_i^{k,j}/N_i$$

Midline · Midline · 1000

Spinal segments: L2, L3, L4, L5, L6, S1

Flexor hotspot · Extensor hotspot

1 · 0

-1500 750 0 1500 · -1500 0 1500

Lateral distance from spinal cord midline (µm)

0.4 0.6 0.8 1.0 · 0.4 0.6 0.8 1.0

Cost to achieve selectivity

Extension hotspot · Flexion hotspot

Supplementary Figure 3: Computer simulations to identify optimal electrode locations to target extensor versus flexor hotspots

(**a**) Spatial distribution of extensor and flexor motoneuron activation profiles along the rostrocaudal extent of lumbar segments. The spatial distribution was extracted using a Gaussian clustering algorithm applied on spatiotemporal maps of motoneuron activation during gait (**Fig. 1a**). (**b**) Equations describing the optimization algorithm that calculated the cost to activate a given spinal segment, while minimizing activation of other segments. The cost function combined four optimization factors: (i) stimulation specificity for the targeted segments; (ii) ipsilateral vs. contralateral specificity; (iii) minimum threshold; and (iv) specificity of neighboring sites. The targeted activation of each segment was defined by the spatial distribution of extensor- and flexor-related motoneuron activation profiles displayed in (a). The color-coded maps report the computed cost to preferentially activate extensor versus flexor hotspots on one side of the spinal cord. Implants were designed with electrodes located at the mediolateral and rostrocaudal positions where the cost reached a local minimum, as highlighted by the black circles.
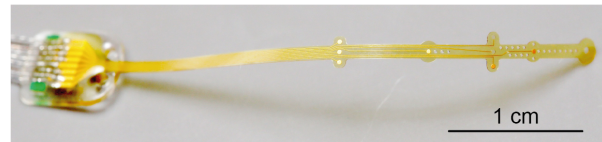
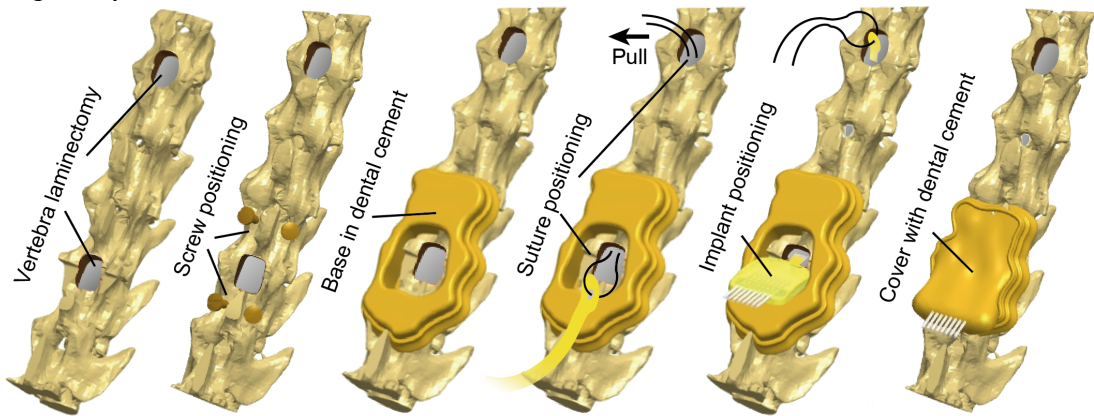# a Design and fabrication of spatially selective spinal implants

Photosensitive
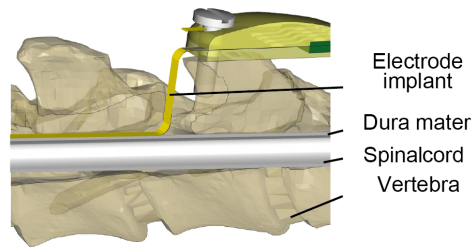Polyimide layer

Polyimide mechanical structure adjustment

Electrode and lead seed pattern

Electroformed electrodes and leads

Polyimide cover layer with openings for
electrodes and contact pads

Wiring and encapsulation

Punctuated holes

b Mask layout

6 (mm)

Electrode: 0.3

0.8   0.75   1

17   2   6.5   5   5

7   35.5

c Final spinal implant with connector

1 cm

d Surgical implantation

Vertebra laminectomy

Screw positioning

Base in dental cement

Suture positioning

Pull

Implant positioning

Cover with dental cement

Vertebral orthosis for epidural implantation in rat

Electrode
implant

Dura mater

Spinalcord

Vertebra

Supplementary Figure 4: Design, fabrication and surgical procedures of spatially selective spinal implants

(**a**) Processing starts with deposition of a 20 μm thick Polyimide film by spin coating on the silicon substrate. The Polyimide-based bottom layer constituting the footprint of the implant is realized through ultra-violet lithography. A 200 nm thick gold layer is deposited using vacuum evaporation and lithographically structured to create a conductive seed pattern. An additional gold layer is electroplated to a height of approximately 6 μm to create the electrodes and interconnects. A 20 μm cover layer of photosensitive Polyimide is then applied by spin coating to uniformly cover the bottom and electrode structure. A final ultra-violet lithography is applied to structure the top layer of the implant, and to create openings over the electrodes and contact pads. The implants are gently released from the carrier wafer. To create a connector, the contact pads located at the extremity of the implant are glued to a small support plate made of medical grade PMMA sheet material. Precision milled alignment structures allow fine adjustment of the support plate to the polyimide-based spinal implant, and to the extremity of the leads. The support plate contained a seat in which a tiny printed circuit board (PCB) with conductive stripes is fixed. Stainless steel leads with silicone rubber insulation are directly soldered to the contact pads of the implant via the contact stripes located on the PCB. The resulting implants and connective leads were highly reliable mechanically and electrically. Finally, the entire contact area was covered with a ultra-violet curable, methacrylate-based resin that provides tight sealing. For improved bio-integration, the contact interface is over-moulded with a thin layer of medical grade silicone. (**b**) Electrode layout and dimensions (mm) of the implants. (**c**) Photograph showing the final fabrication of the spinal implants. (**d**) Under sterile conditions, a dorsal midline skin incision was made and the muscles covering the dorsal vertebral column were removed. A partial laminectomy was made at vertebrae levels L3–L4 in rats and L4–L5 in monkeys, and at vertebrae T12–T13 to create entry and exit points for the implant. In rats and mice, four micro-screws were then inserted into the bone of vertebrae L4 and L5, at the entry points of the laminectomy. Surgical suture was used to form walls around the micro-screws. The walls were plastered using freshly mixed dental cement, which formed a vertebral fixation structure and protective cage for the spinal implant. A surgical suture (Ethilon 4.0) was folded to form a loop that was inserted through the rostral (T12–T13) laminectomy (above or below the dura mater), and pushed horizontally along the epidural space until the loop emerged through the caudal (L4 or L5) opening. The suture was passed through a hole created at the extremity of the Polyimide-based spinal implant. The loop was gently retracted to position the implant over the desired spinal cord location. A small portion of the implant protruded outside the spinal canal. Using fine-forceps, the extremity of the implant was displaced along the mediolateral and rostrocaudal directions to fine-tune its positioning. For this, single pulses were delivered through the electrodes targeting extensor and flexor hotspots. The mediolateral position of the implant was adjusted to obtain unilateral motor responses with both sets of lateral electrodes. The rostrocaudal position of the implant was adjusted to obtain selective movement of ankle extension and hip flexion with electrodes targeting extensor versus flexion hotspots, respectively. For fine positioning, we also monitored motor evoked potentials in an ankle extensor muscle and a hip flexor muscle of the left and right hindlimbs. The connector was positioned within the cage and an additional layer of dental cement was added to close the vertebral fixation structure. The Teflon-insulated stainless steal wires soldered to the connector were routed subcutaneously to the head of the rat. The wires were soldered to an Omnetics electrical connector that was secured to the skull using dental cement.
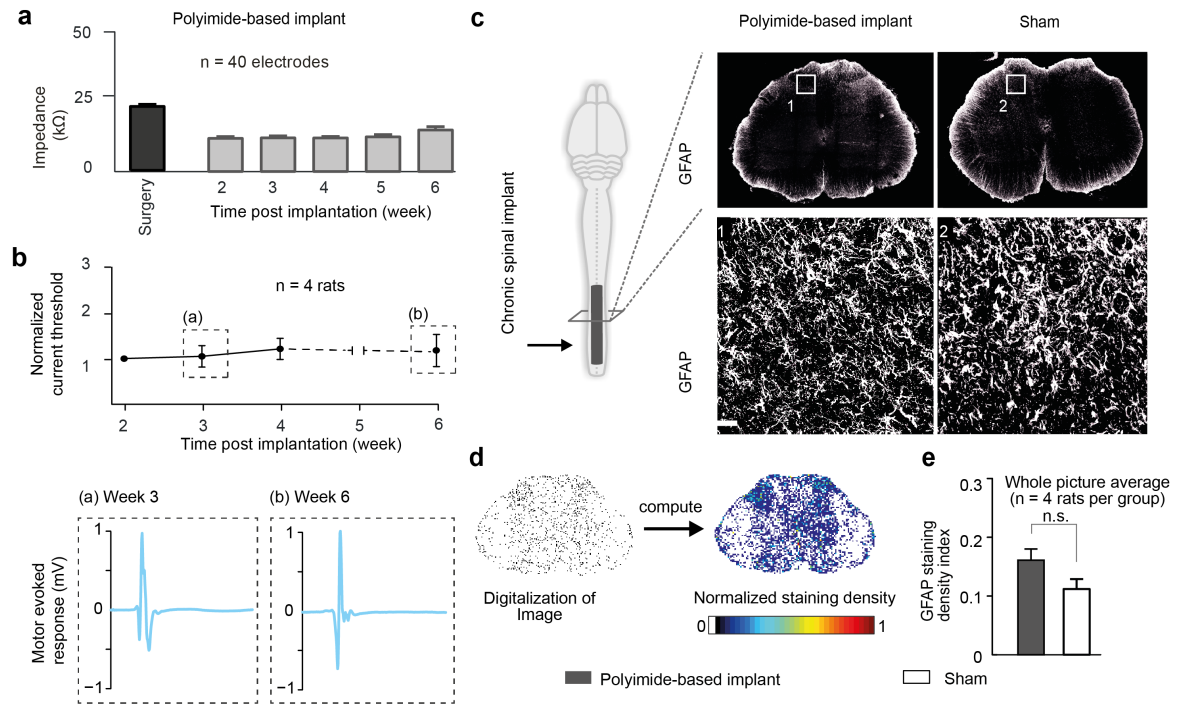
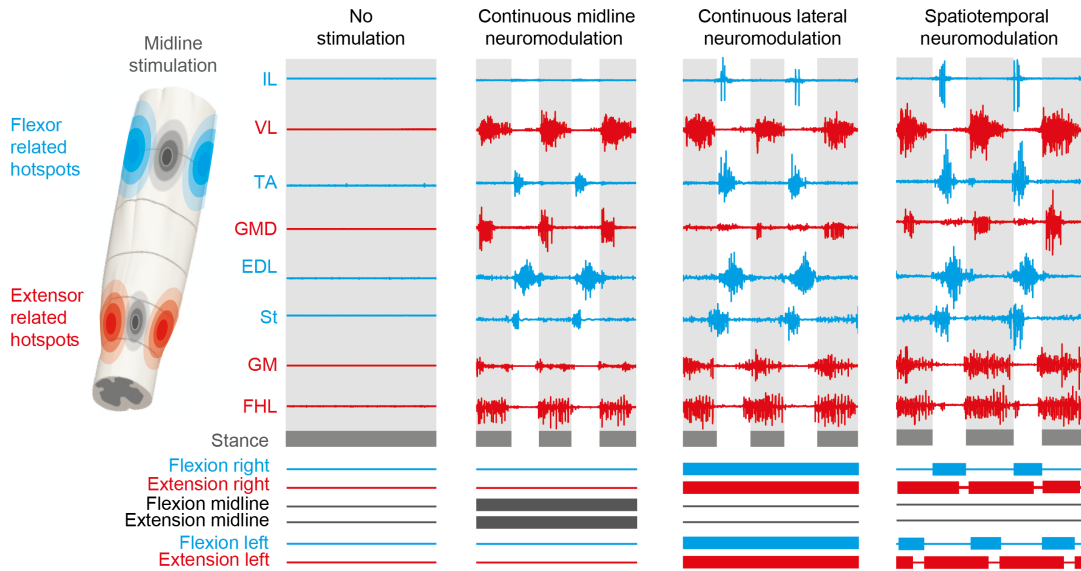**Supplementary Figure 5: Long-term functionality and bio-integration of epidural spinal implants**
(**a**) Histogram plots reporting changes in the mean values of electrode impedance of polyimide-based epidural spinal implants in rats. The impedance was measured for all the electrodes of the implants in the same rats during the surgical implantation, and on a weekly basis during the subsequent weeks. (**b**) Plots reporting the normalized current threshold necessary to elicit motor evoked responses in the tibialis anterior muscle with a single pulse of electrical stimulation (0.5 ms, 0.1 Hz) delivered through the same electrode over several weeks post implantation. Measurements could not be obtained on week 5 due to technical problems. The windows display motor evoked responses recorded in the tibialis anterior muscle at week 3 and week 6 post-implantation when delivering stimulation at 150 µA through the same electrode of the spinal implant. (**c**) Rats (*n* = 4 per group) were sacrificed 8 weeks after the surgical insertion of Polyimide-based spinal implants over the epidural surface of lumbosacral segments. Representative confocal images of the L4 spinal segment (middle of implant) stained for the neuro-inflammatory marker GFAP (reactive astrocytes) are shown for the implanted and sham rats. Scale bars, 500 µm and 40 µm for the overviews and insets, respectively. (**d**) Images were digitalized, color-filtered, and binarized by means of an intensity threshold that was maintained constant across sections and rats. Images were divided into square regions of interest (ROI), and GFAP densities were computed within each ROI. (**e**) Histogram plots reporting the mean and SEM values of computed GFAP density for rats with spinal implants and sham rats. Spinal implants had a negligible impact on the inflammatory environment of spinal tissue located underneath the implant. n.s. = non-significant.
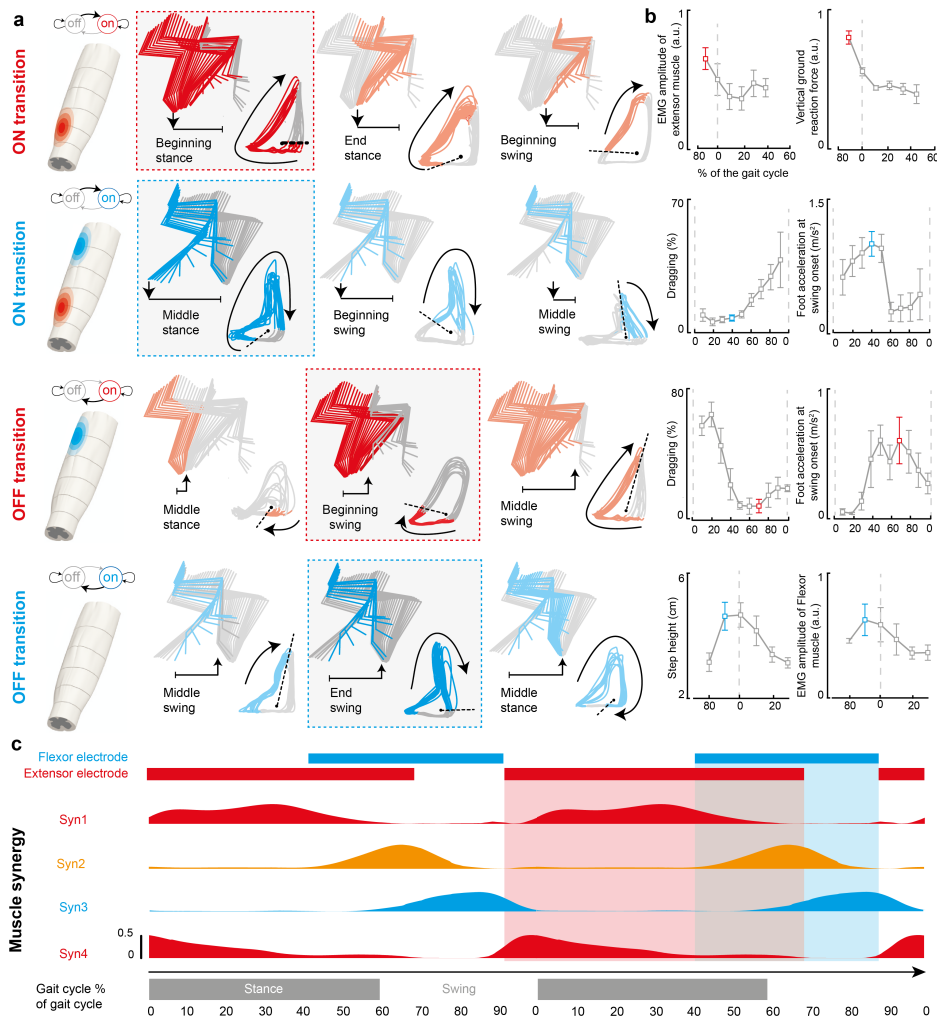
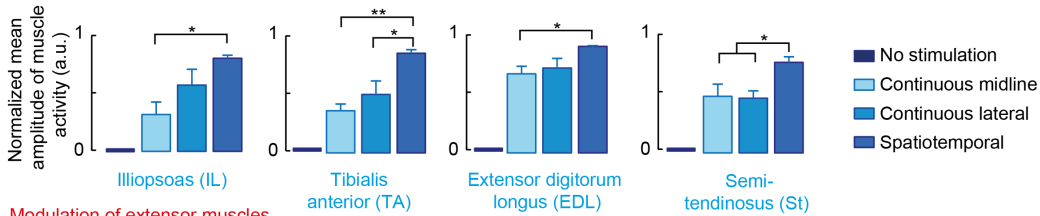**Supplementary Figure 6: Experiments to identify optimal temporal structure**
(**a**) Experiments were performed in rats with complete SCI. A serotonergic replacement therapy was administered 10 min prior to experiments. Rats stepped bipedally on a treadmill while neuromodulation (40 Hz, 0.2 ms, 100–200 μA) was delivered through the electrodes targeting extensor versus flexor hotspots on one side. The spinal cord diagrams illustrate the intended activation or inactivation of a given hotspot. The lines with an arrowhead indicate the onset (beginning of line) and end (arrowhead) of the stimulation. The arrowhead highlights the timing of the transition between states represented in each panel. A stick diagram decomposition of hindlimb movements during a complete gait cycle is displayed for three selected triggering times per transition state. The successive (*n* = 10 steps) trajectories of the hindlimb endpoint are also reported. Both stick diagrams and hindlimb endpoint trajectories are colored when the state of the tested electrode is ON. The dotted line indicates the angular value that triggered the transition between ON–OFF states, reported as percent of the gait cycle duration. The shaded background highlights the optimal triggering time, defined from combinations of parameters (see **Methods**). (**b**) Plots reporting the mean values (10 steps per data point, n = 5 rats) of relevant gait parameters related to extension or flexion across the entire range of tested triggering times. For each rat, the normalized gait cycle duration was divided into 10 bins of equal durations, reported along the x-axis as percent of cycle duration. The triggering times leading to optimal gait parameters are colored in red and blue for electrodes targeting extensor and flexor hotpots, respectively. (**c**) Diagram reporting the optimal temporal structure to deliver stimulation through the electrodes targeting extensor versus flexor hotspots in order to facilitate locomotion. The temporal activation profiles of muscle synergies are displayed at the bottom to emphasize the coincidence between the optimal temporal structure of stimulation and the activation of muscle synergies. Note that the optimal temporal structure involved co-activation of electrodes targeting the extensor and flexor hotspots at the stance to swing transition, which coincided with the activation of synergy 2 combining extensor and flexor motoneurons (see **Fig. 1**). The lower bar indicates the division of gait into bins of equal durations that defined the timing to trigger events.

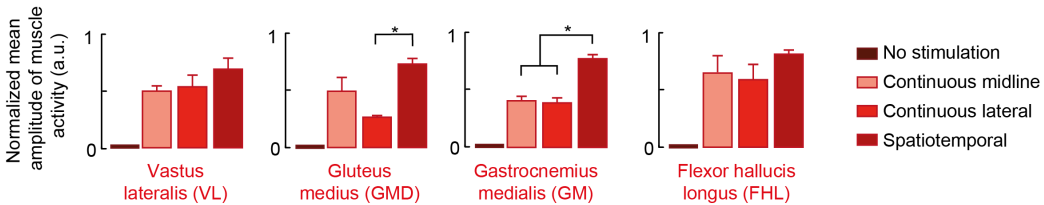**a Muscle activity during locomotion under different neuromodulation conditions**

Midline stimulation

Flexor related hotspots

Extensor related hotspots

No stimulation | Continuous midline neuromodulation | Continuous lateral neuromodulation | Spatiotemporal neuromodulation

IL
VL
TA
GMD
EDL
St
GM
FHL
Stance
Flexion right
Extension right
Flexion midline
Extension midline
Flexion left
Extension left

b Quantification of muscle activity

Modulation of flexor muscles

Normalized mean amplitude of muscle activity (a.u.)

Illiopsoas (IL) Tibialis anterior (TA) Extensor digitorum longus (EDL) Semi-tendinosus (St)

No stimulation
Continuous midline
Continuous lateral
Spatiotemporal

Modulation of extensor muscles

Normalized mean amplitude of muscle activity (a.u.)

Vastus lateralis (VL) Gluteus medius (GMD) Gastrocnemius medialis (GM) Flexor hallucis longus (FHL)

No stimulation
Continuous midline
Continuous lateral
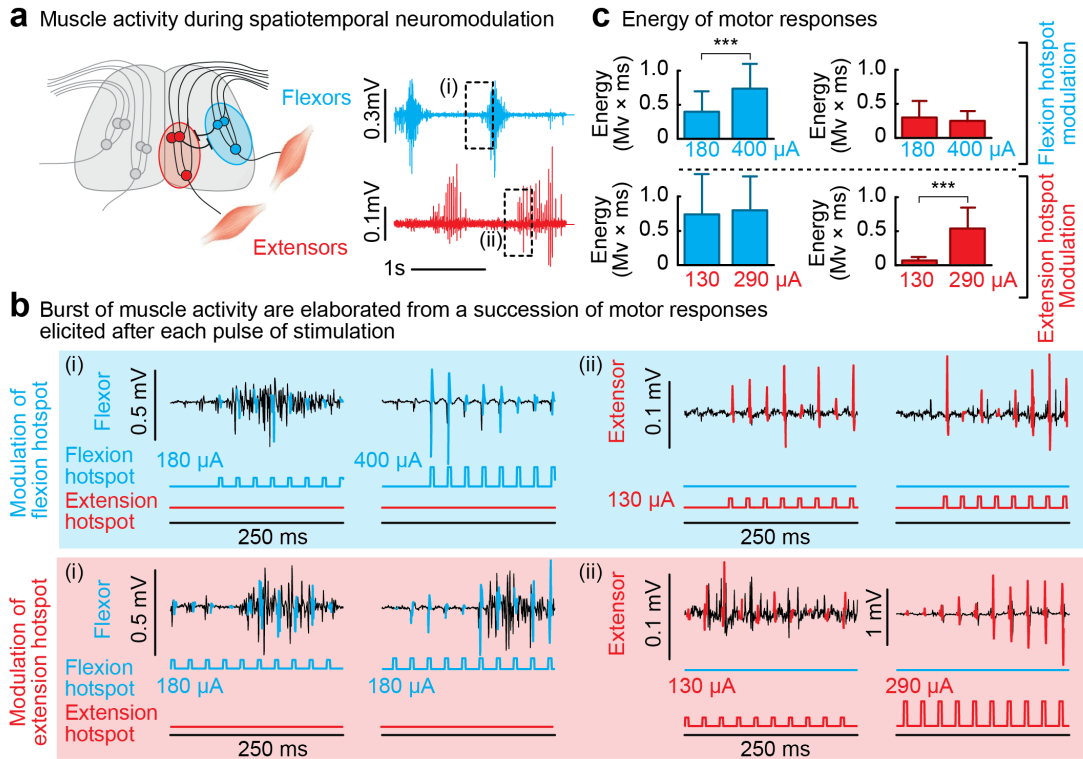Spatiotemporal

Supplementary Figure 7: Changes in hindlimb muscle activity across conditions of neuromodulation

(**a**) Electromyographic activity recorded from pairs of antagonist muscles spanning each hindlimb joint without stimulation (paralysis), during locomotion under continuous neuromodulation applied over the midline of lumbar and sacral segments, during continuous neuromodulation delivered through all the four lateral electrodes targeting extensor and flexor hotspots on the left and right sides, and during spatiotemporal neuromodulation through the lateral electrodes using the temporal structure identified in **Supplementary Fig. 6**. The recordings were obtained on the same day. The horizontal bars at the bottom (blue, red, black) indicate the On/Off state of each electrode, which is controlled in real-time. Experimental conditions and conventions are the same as in **Fig. 4**. (**b**) Histogram plots reporting the mean ($n = 4$ rats, except $n = 5$ rats for MG and TA muscles) amplitude of each muscle burst during each experimental condition. The mean amplitude of EMG activity was normalized to the maximum value recorded during locomotion in each rat. *, $P < 0.05$; **, $P < 0.01$.
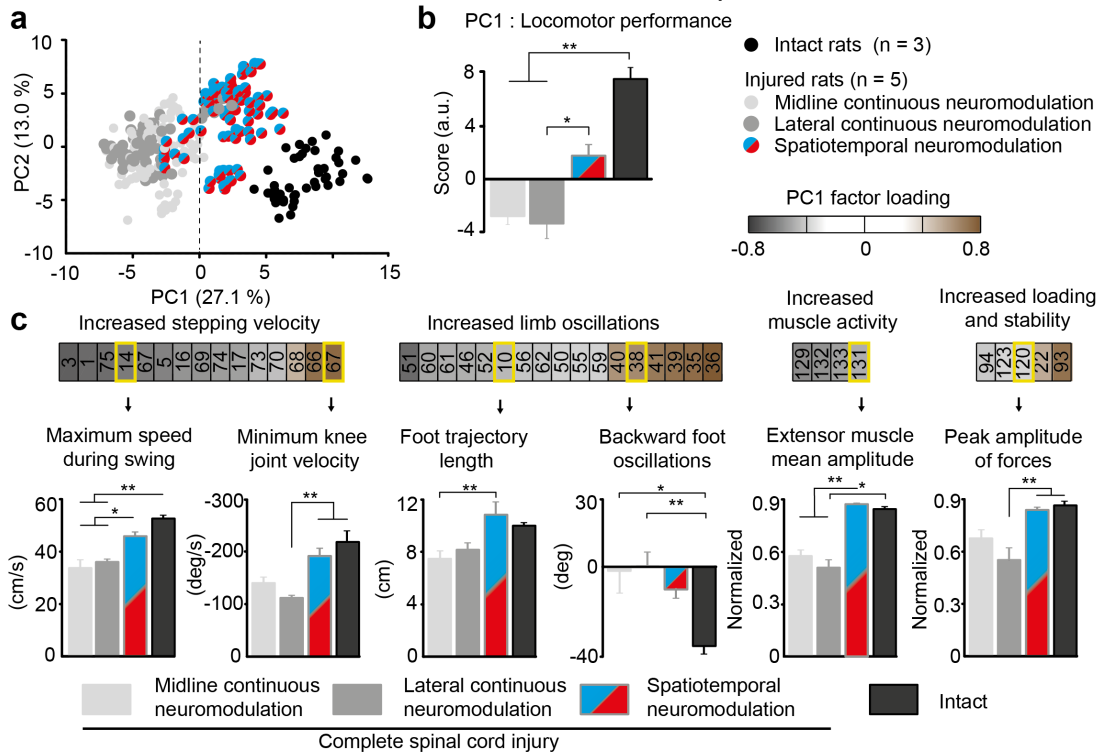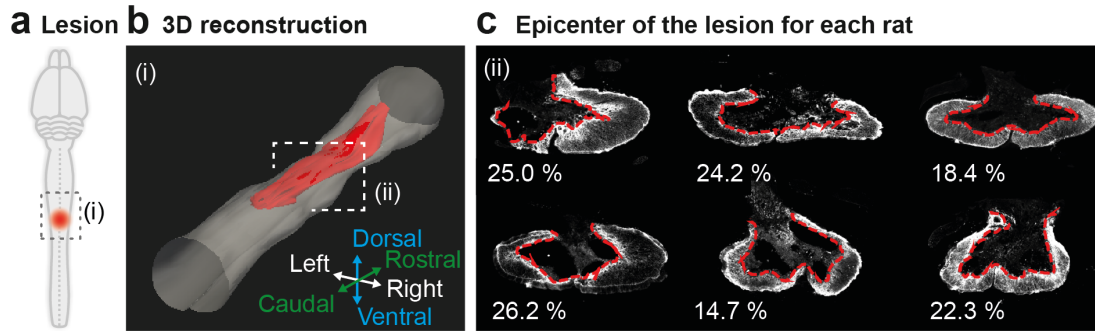
Supplementary Figure 8: Quantification of gait patterns in rats with complete SCI
(**a**) A total of 137 parameters providing comprehensive gait quantification (**Supplementary Table 1**) were computed from kinematic, kinetic, and muscle activity recordings. Principal component (PC) analysis was applied on all the computed parameters for all the gait cycles under each experimental condition. Experimental conditions are the same as in **Fig. 4**. The analyzed gait cycles are represented by individual dots in the new 2D space created by PC1-2, which explained more than 40 % of the total data variance. The histogram plots report the mean values of scores on PC1, which quantified the degree of difference between gait patterns of intact and injured rats during locomotion under the various experimental conditions. Scores on PC1 are thus related to locomotor performance. This analysis demonstrated significant improvement of locomotor performance during spatiotemporal neuromodulation compared to continuous neuromodulation applied over the midline, or through lateral electrodes targeting extensor versus flexor hotspots. (**b**) To identify the specific features that improved during spatiotemporal neuromodulation, the parameters correlating with PC1 (factor loadings) were extracted and regrouped them into functional clusters, which are named for clarity. The numbers refer to parameters described in **Supplementary Table 1**. (**c**) The histogram plots report the mean ($n = 5$ rats) values of parameters with high factor loadings on PC1 for each of the identified functional clusters. Error bars, SEM. *, $P < 0.05$; **, $P < 0.01$.

a Muscle activity during spatiotemporal neuromodulation

Flexors

Extensors

c Energy of motor responses

Flexion hotspot modulation

Extension hotspot Modulation

b Burst of muscle activity are elaborated from a succession of motor responses elicited after each pulse of stimulation

Modulation of flexion hotspot

Modulation of extension hotspot

Supplementary Figure 9: Modulation of motor responses during increase in stimulation amplitude

(**a**) The diagram shows the proprioceptive feedback circuits that are thought to be recruited by epidural electrical stimulation. Electromyographic activity of flexor and extensor ankle muscles is shown for two successive steps performed under spatiotemporal neuromodulation. The dashed rectangles (i) and (ii) highlight the temporal window over which the muscle activity is displayed below. (**b**) Extensor and flexor muscle activity recorded with two levels of stimulation amplitudes for the electrode targeting the extensor versus flexor hotspot. Motor responses resulting from each stimulation pulse, indicated below each trace, are shown in color. (**c**) Histogram plots reporting the mean energy of motor responses in flexors and extensors muscles for the different experimental conditions. Energy was calculated as the square root of the second power of the signal, which was integrated over 2 ms. Bars show the median and 75% of the distribution. Non-parametric ANOVA statistical test was applied over 3000 responses. ***, $P < 0.001$.

a Lesion **b** 3D reconstruction

c Epicenter of the lesion for each rat

Supplementary Figure 10: Quantification of spared tissue in rats with contusion SCI
(**a**) Diagram illustrating the contusion SCI at the mid-thoracic level. (**b**) 3D reconstruction of a lesion cavity. (**c**) Photograph of coronal spinal cord sections taken at the lesion epicenter for each experimental rat. The tissues are stained against GFAP (reactive astrocyte) in order to delimitate the border between the lesioned and healthy tissues, shown with the red dashed lines. The calculated percent of tissue sparing is reported for each rat.

a Quadrupedal locomotion on runway

— Stance
— Drag
— Swing
— Trunk balance
— Endpoint trajectory
● Maximal step height

5cm

10cm

No stimulation

Spatiotemporal neuromodulation

b

PC2 (12 %)

PC1 (17.6 %)

c PC1 : Locomotor performance

Score (a.u.)

● Intact rats (n = 4)
Injured rats (n = 6)
○ No stimulation
◑ Spatiotemporal neuromodulation

PC1 factor loading

-1   0   1

d

Stepping velocity
69 75 71 73 2 70 65 67
↓
Knee joint angle velocity

Endpoint trajectory
9 14 10 13 17 16 9 12
↓   ↓
Step Heigth   Dragging

Limb oscillation
59 61 57 42 51 63
↓
Knee joint angle amplitude

Loading and stability
23 28 27 24 22
↓
Step width

(m/s)   *** *
18
12
6
0

(cm)   ***
2   *
1
0

(%)   ***
50   **
25
0

(deg)   *
50
25
0

(cm)   ***
8   *
4
0

☐ No stimulation   ◤ Spatiotemporal neuromodulation   ■ Intact

Spinal cord contusion

Supplementary Figure 11: Quantification of locomotor performance during quadrupedal locomotion

(**a**) Stick diagram decomposition of hindlimb and trunk movements together with hindlimb endpoint trajectory during quadrupedal locomotion without stimulation and under spatiotemporal neuromodulation. Rats were recorded 2 months after the contusion SCI, when recovery had plateaued. (**b**) A PC analysis was applied using same methods as those described in **Supplementary Fig. 8,** and displayed with the same convention as in this figure. Error bars, SEM. *, $P < 0.05$; **, $P < 0.01$; ***, $P < 0.001$.

Supplementary Table 1: Computed kinematic, kinetic, and muscle activity parameters

PARAMETERS	LABEL #	EXPLANATION OF PARAMETERS
KINEMATIC VARIABLES		
Temporal features		
	1	Cycle duration
	2	Cycle velocity
	3	Stance duration
	4	Swing duration
	5	Relative stance duration (percent of the cycle duration)
Limb endpoint (Metatarsal phalange) trajectory		
	6	Interlimb temporal coupling
	7	Duration of double stance phase
	8	Stride length
	9	Step length
	10	3D limb endpoint path length
	11	Maximum backward position
	12	Minimum forward position
	13	Step height
	14	Maximum speed during swing
	15	Relative timing of maximum velocity during swing
	16	Acceleration at swing onset
	17	Average endpoint velocity
	18	Orientation of the velocity vector at swing onset
	19	Dragging
	20	Relative dragging duration (percent of swing duration)
Stability		
Base of support	21	Positioning of the foot at stance onset with respect to the pelvis
	22	Stance width
Trunk and pelvic	23	Maximum hip sagittal position
	24	Minimum hip sagittal position
position and	25	Amplitude of sagittal hip oscillations
	26	Variability of sagittal crest position
oscillations	27	Variability of sagittal crest velocity
	28	Variability of vertical hip movement
	29	Variability of sagittal hip movement
	30	Variability of the 3D hip oscillations
	31	Length of pelvis displacements in the forward direction
	32	Length of pelvis displacements in the medio-lateral direction
	33	Length of pelvis displacements in the vertical direction
	34	Length of pelvis displacements in all directions
Joint angles and segmental oscillations		
Backward	35	Crest oscillations
	36	Thigh oscillations
	37	Leg oscillations
	38	Foot oscillations
	39	Whole limb oscillations
Forward	40	Crest oscillations
	41	Thigh oscillations
	42	Leg oscillations
	43	Foot oscillations
	44	Whole limb oscillations
Flexion	45	Hip joint angle
	46	Knee joint angle
	47	Ankle joint angle
Abduction	48	Whole limb abduction
	49	Foot abduction
Extension	50	Hip joint angle
	51	Knee joint angle
	52	Ankle joint angle
Adduction	53	Whole limb adduction
	54	Foot adduction
Amplitude	55	Crest oscillations

	56	Thigh oscillations
	57	Leg oscillations
	58	Foot oscillations
	59	Whole limb oscillations
	60	Hip joint angle
	61	Knee joint angle
	62	Ankle joint angle
	63	Whole limb medio-lateral oscillations
	64	Foot abduction/adduction
Velocity		
Minimum	65	Whole limb oscillation velocity
	66	Hip joint angle velocity
	67	Knee joint angle velocity
	68	Ankle joint angle velocity
Maximum	69	Whole limb oscillation velocity
	70	Hip joint angle velocity
	71	Knee joint angle velocity
	72	Ankle joint angle velocity
Amplitude	73	Whole limb angle velocity
	74	Hip joint angle velocity
	75	Knee joint angle velocity
	76	Ankle joint angle velocity
Inter-limb coordination		
PC analysis	77	Degree of linear coupling between joint oscillations
FFT	78	Temporal coupling between crest and thigh oscillations
decomposition	79	Temporal coupling between thigh and leg oscillations
	80	Temporal coupling between leg and foot oscillations
	81	Correlation between crest and tight oscillations
	82	Correlation between tight and leg oscillations
	83	Correlation between leg and foot oscillations
Cross-correlation	84	Correlation between hip and knee oscillations
	85	Correlation between knee and ankle oscillations
	86	Correlation between ankle and MTP oscillations
	87	Temporal lag between backward positions of crest and thigh oscillations
	88	Temporal lag between forward positions of crest and thigh oscillations
Relative coupling	89	Temporal lag between backward positions of thigh and leg oscillations
	90	Temporal lag between forward positions of the thigh and leg oscillations
	91	Temporal lag between backward positions of leg and foot oscillations
	92	Temporal lag between forward positions of leg and foot oscillations
	93	Lag of the cross correlation function between hindlimb oscillations
Inter-segmental coordination	94	Maximum R-value of the cross correlation function between hindlimb oscillations
compared to	95	Lag of the cross correlation function between hip oscillations
	96	Maximum R-value of the cross correlation function between hip oscillations
Able-bodied rats		
	97	Lag of the cross correlation function between knee oscillations
	98	Maximum R-value of the cross correlation function between knee oscillations
	99	Lag of the cross correlation function between ankle oscillations
	100	Maximum R-value of the cross correlation function between ankle oscillations
	101	Lag of the cross correlation function between endpoint oscillations
	102	Maximum R-value of the cross correlation function between endpoint oscillations
	103	Phase of the first harmonic of the FFT of the hip elevation angle
	104	Amplitude of the first harmonic of the FFT of the hip elevation angle
	105	Phase of the first harmonic of the FFT of the knee elevation angle
	106	Amplitude of the first harmonic of the FFT of the knee elevation angle
	107	Phase of the first harmonic of the FFT of the ankle elevation angle
	108	Amplitude of the first harmonic of the FFT of the ankle elevation angle
Left–right	109	Phase of the first harmonic of the FFT of the endpoint elevation angle
	110	Amplitude of the first harmonic of the FFT of the endpoint elevation angle
hindlimb	111	Phase of the first harmonic of the FFT of the hindlimb elevation angle
	112	Amplitude of the first harmonic of the FFT of the hindlimb elevation angle

coordination	113	Lag of the cross correlation function between crest and thigh limb elevation angles
Hindlimb	114	Lag of the cross correlation function between thigh and hindlimb elevation angles
coordination	115	Lag of the cross correlation function between hip and thigh elevation angles
	116	Lag of the cross correlation function between hindlimb and foot elevation angles
	117	Lag of the cross correlation function between thigh and ankle elevation angles
	118	Lag of the cross correlation function between ankle and foot elevation angles

KINETIC VARIABLES

	119	Mean amplitude of vertical forces (normalized to maximum value)
	120	Peak amplitude of vertical forces (normalized to maximum value)
	121	Peak to peak amplitude of vertical forces (normalized to maximum value)
	122	
	123	Root mean square of vertical forces (normalized to maximum value)
		Integral of vertical forces (normalized to maximum value)
	124	Weight-bearing level

MUSCLE ACTIVITY VARIABLES

Timing (relative to cycle duration, paw contact to paw contact)

Extensor	125	Relative onset of ipsilateral extensor muscle activity burst
	126	Relative end of ipsilateral extensor muscle activity burst
Flexor	127	Relative onset of ipsilateral flexor muscle activity burst
	128	Relative end of ipsilateral flexor muscle activity burst

Duration

Extensor	129	Duration of ipsilateral extensor muscle activity burst
Flexor	130	Duration of ipsilateral flexor muscle activity burst

Amplitude

Extensor	131	Mean amplitude of ipsilateral muscle activity burst
	132	Integral of ipsilateral extensor muscle activity burst
	133	Root mean square of ipsilateral extensor muscle activity burst
Flexor	134	Mean amplitude of ipsilateral flexor muscle activity burst
	135	Integral of ipsilateral flexor muscle activity burst
	136	Root mean square of ipsilateral flexor muscle activity burst
Muscle coactivation	137	Co-contraction of flexor and extensor muscle

Supplementary Table 2: Detailed information on sample descriptions and statistics

		Sample		Statistics		
	Description	size	Methods	Reported	P-values
Figure 2c	Vertical displacement of the leg in acute condition	flexor hotspot(A))= 4 targeted leg movements / 6 rats	One-Way ANOVA	mean +/- SEM	1.72E-07
		flexor hotspot(B))= 4 untargeted leg movements / 6 rats			
		Extensor hotspot(C))= 4 targeted leg movements / 6 rats			
		Extensor hotspot(D))= 4 untargeted leg movements / 6 rats			
Figure 4c	Peak amplitude of vertical forces	Midline continuous neuromodulation (A) = 10 steps / 5 rats	Kurskal Wallis	mean +/- SEM	0.00328
		Lateral continuous neuromodulation (B) = 10 steps / 5 rats			
		Spatiotemporal neuromodulation (C) = 10 steps / 5 rats			
		Intact rat(D) = 10 steps / 3 rats			
Figure 4c	Peak velocity during swing	Midline continuous neuromodulation (A) = 10 steps / 5 rats	Kurskal Wallis	mean +/- SEM	0.0042
		Lateral continuous neuromodulation (B) = 10 steps / 5 rats			
		Spatiotemporal neuromodulation (C) = 10 steps / 5 rats			
		Intact rat(D) = 10 steps / 3 rats			
Figure 5b	Ground reaction force during stance	Extensor amplitude 1.2 = 10 steps / 5 rats	One-Way ANOVA	mean +/- SEM	0.007
		Extensor amplitude 1.6 = 10 steps / 5 rats			
		Extensor amplitude 2.1 = 10 steps / 5 rats			
		Extensor amplitude 2.5 = 10 steps / 5 rats			
Figure 5b	Normalized Step height during swing	Flexor amplitude 1.2 = 10 steps / 5 rats	One-Way ANOVA	mean +/- SEM	0.0316
		Flexor amplitude 1.6 = 10 steps / 5 rats			
		Flexor amplitude 2.1 = 10 steps / 5 rats			
		Flexor amplitude 2.5 = 10 steps / 5 rats			
Figure 6c	Maximum weight bearing	Continuous neuromodulation = 6 rats	Paired t-test	mean +/- SEM	0.0012
		Spatiotemporal neuromodulation = 6 rats			
Figure 6c	Peak force at foot strike	Continuous neuromodulation = 10 steps /6 rats	Paired t-test	mean +/- SEM	0.0246
		Spatiotemporal neuromodulation = 10 steps / 6 rats			
Figure 6c	Amplitude of extensor muscle	Continuous neuromodulation = 10 steps / 6 rats	Paired t-test	mean +/- SEM	0.0156
		Spatiotemporal neuromodulation = 10 steps / 6 rats			
Figure 6d	Time until collapse on treadmill	Continuous neuromodulation = 6 rats	Paired t-test	mean +/- SEM	0.0095
		Spatiotemporal neuromodulation = 6 rats			
Figure 6e	Trunk Index	No neuromodulation = 10 steps / 6 rats	Paired t-test	mean +/- SEM	0.0011
		Spatiotemporal neuromodulation = 10 steps / 6 rats			
Figure 6f	Staircase success rate	No neuromodulation = 12 step /6 rats	Paired t-test	mean +/- SEM	0.008
		Spatiotemporal neuromodulation = 12 step / 6 rats			